Flow Turbulence Combust (2012) 88:101–120
DOI 10.1007/s10494-011-9379-3

Turbulent Heat Transfer and Large Coherent Structures in Trailing-edge Cutback Film Cooling

Hayder Schneider · Dominic von Terzi · Hans-Jörg Bauer

Received: 18 November 2010 / Accepted: 20 October 2011 / Published online: 11 November 2011

Abstract Film cooling is a key technology for improving the thermal efficiency and power output of gas turbines. The trailing-edge section of high-pressure turbine blades can be efficiently cooled by ejecting a film over a cutback on the pressure side of the blade. In this paper, results of Large–Eddy Simulations (LES) are presented that match an existing experimental setup. Altogether, eight simulations with the blowing ratio M varying as the only parameter were performed over a range from $M = 0.35$ to 1.4. Reasonably good agreement between LES and experiments were obtained for flow field statistics and adiabatic film-cooling effectiveness η_{aw}. Within a limited range of blowing ratios, an increase in the blowing ratio results in a counter-intuitive decrease of the cooling effectiveness. The present work suggests a mechanism that can explain this behavior. The visualization and analysis of large coherent structures showed that there exists dominant clockwise-rotating structures that can give rise to a combined upstream- and wall-directed turbulent heat flux. This turbulent heat flux represents the main contribution of the total heat flux and causes a significantly intensified thermal mixing process, which in turn results in the counter-intuitive decrease of the cooling effectiveness.

Keywords Large–Eddy simulation · Large coherent structures · Turbulent mixing · Heat transfer · Film cooling

1 Introduction

Film cooling is a key technology for improving the performance of gas turbines. The aim of film cooling is to increase the maximum allowable turbine inlet temperature,

H. Schneider (✉) · D. von Terzi · H.-J. Bauer
Institut für Thermische Strömungsmaschinen, Karlsruhe Institute of Technology (KIT),
Kaiserstr. 12, 76131 Karlsruhe, Germany
e-mail: hayder.schneider@kit.edu

which implicates an increase in thermal efficiency and power output, but also an extension of the durability and life of turbine components. The trailing-edge (TE) section of high-pressure turbine blades, see Fig. 1a, is subject to large heat loads and therefore requires substantial cooling efforts. An efficient cooling method for the TE is cutback film cooling, where cooling air is ejected over a cutback on the pressure side of the blade. Since the cooling air must be extracted from earlier compressor stages it does not perform work and, thus, amounts for a thermodynamic loss. Consequently, the design goal is to minimize the cooling air flow while still ensuring acceptable component temperatures.

The key quantity for assessing the film cooling performance of a particular laboratory configuration is the adiabatic film cooling effectiveness η_{aw}. This quantity is mainly influenced by the geometrical features of the TE cutback, the blowing ratio M and the coolant channel flow characteristics. For incompressible, constant property flow, η_{aw} is defined as

$$\eta_{\mathrm{aw}} = \frac{T_{\mathrm{h}} - T_{\mathrm{aw}}}{T_{\mathrm{h}} - T_{\mathrm{c}}}, \tag{1}$$

where T is the averaged temperature and the idices 'aw', 'h', and 'c' refer to the temperatures of the adiabatic wall, the hot gas path, and the coolant channel, respectively. The blowing ratio is defined as

$$\mathrm{M} = \frac{(\rho U)_{\mathrm{c}}}{(\rho U)_{\mathrm{h}}}, \tag{2}$$

where ρ is the density and U the bulk velocity in the streamwise direction. Other influencing parameters include transitioning boundary layers, free-stream turbulence, secondary flows, and rotational effects; a more complete list is provided by Bunker [1]. The large number of influencing parameters requires systematic parameter studies for the optimization of the cooling design. Experimental parameter studies are generally very expensive and often subject to severe measurement limitations. This motivates the use of numerical prediction methods which can provide more details about the flow physics and, ultimately, can lead to cooling design optimizations by exploiting the physical mechanisms at work.

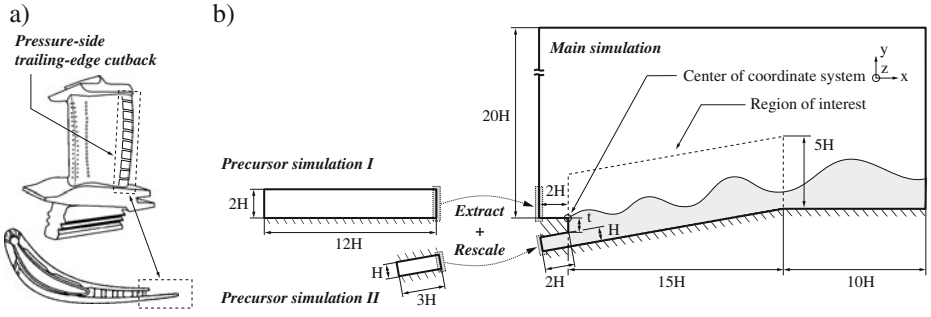

Fig. 1 Trailing-edge cutback: **a** three-dimensional view (*top*) and cross-sectional view (*bottom*). **b** Schematic of the part of the experimental setup computed with flow from *left to right* and the *grey shaded area* indicating the coolant flow, taken with permission from [12]

The flow physics in TE cutback film cooling is governed by the formation of large coherent structures (LCS) which are periodically shed at the blunt cutback lip. These LCS dominate the mixing process and, subsequently, impact on the film cooling effectiveness. Because large-scale unsteadiness is so important for the mixing process, the Large–Eddy Simulation (LES) approach is conceptually the ideal calculation method for accurately and reliably predicting both the flow field and heat transfer. However, until recently, the more cost-efficient Reynolds-Averaged Navier–Stokes (RANS) [2–4] and hybrid LES/RANS [5, 6] calculation methods were used for predicting TE cutback film cooling; see for an overview on RANS and LES, and on hybrid LES/RANS methods the work of Pope [7], and of Fröhlich and von Terzi [8], respectively. Holloway et al. [2, 3], and Medic and Durbin [4] used unsteady RANS calculations and obtained a significant overprediction of the adiabatic film cooling effectiveness η_{aw}. Joo and Durbin [5] studied the reason for this overprediction and found that the near-wall processes are misrepresented by the selected RANS method. On the other hand, their hybrid LES/RANS calculation agreed reasonably well with the experimental data of Holloway et al. [2]. Martini et al. investigated experimentally [9, 10] and numerically [6] how internal cooling designs impact on film cooling. Note that internal cooling designs typically consist of so-called turbulators or pin-fins, and are important for the internal convective cooling which is applied prior to ejecting the cool gas onto the TE cutback [1]. Their hybrid LES/RANS calculations agreed reasonably well with the experimental data and it was found that internal cooling designs strongly influence the mixing process and, hence, the film cooling effectiveness. In recent experiments, Horbach [11] studied various lip thickness', lip shapes, and pin fin geometries in a setup with and without land extensions and confirmed the strong influence of these parameters on both film cooling effectiveness and heat transfer.

Martini [10] also conducted reference experiments without land extensions and internal cooling designs. Recently, Schneider et al. [12] reported on highly-resolved LES of these experiments and established the scenario of reducing the blowing ratio from an engine-typical to a lower value by considering also a possible relaminarization of the cool gas flow. Reasonably good agreement of mean velocity profiles and η_{aw} with the experimental data was obtained. It was shown that changing either the blowing ratio or the flow regime of the cool gas flow can change both the type and the strength of the LCS. The change in LCS had significant consequences for the mixing process: it was possible to obtain a counter-intuitive increase in η_{aw} for the reduced blowing ratio. This counter-intuitive increase was also observed in the experiments [9, 10]. So far, the origin of this increase has been unclear, but it is conjectured to be related to LCS. Therefore, in the present study, calculations for a wide range of blowing ratios were conducted with the aim to further the understanding of this phenomena.

2 Computational Setup

2.1 Experiment simulated

Figure 1b depicts the computational domain and its dimensions which represent a part of the experiment of Martini [10]. The geometry and Reynolds number are in

accordance with the reference experiments with zero main flow acceleration along the trailing edge and without lands and internal cooling designs. The lip thickness t to slot height H ratio of $t/H = 1$. All values reported are made dimensionless using H and bulk values of the hot gas at the inlet. The Reynolds number based on H, the hot gas bulk velocity U_h and kinematic viscosity ν_h is 6,250. The Prandtl number is 0.71 and the Mach number was below 0.15. The center of the Cartesian coordinate system was placed at the upper corner of the cutback lip. The hot gas flow enters the domain $2H$ upstream the cutback lip with U_h and temperature T_h. The coolant flow with bulk velocity U_c and temperature T_c passages an inclined channel with length $2H$ and angle of incidence $\alpha = 10°$.

It should be noted that the experiments of Martini [10] were performed as part of the European research project AITEB–2 "Aerothermal Investigations of Turbine Endwalls and Blades". All important parameters such as geometry and flow conditions were determined by a consortium of both gas turbine manufacturers and universities in order to ensure the engineering relevance. The Reynolds number and lip thickness to slot height ratio are typical for a turbine. Although the reference case may seem oversimplified at first, it is useful as it appoximates a wide range of other trailing-edge designs. When looking at internal designs, these are located upstream to the ejection slot and have a lateral spacing. In the case of a sufficiently large upstream distance (say several H) from the ejection slot and/or when the spacing is large between these designs, the geometry approaches the reference case. The same is true when land extensions have a large lateral spacing. Hence, even though the geometry is simplified, it is still of high practical relevance for turbine design.

2.2 Numerical method and subgrid-scale model

The three-dimensional, time-dependent, filtered Navier–Stokes equations governing incompressible, constant-property flow were solved using the Finite Volume in-house code LESOCC2 developed at KIT; see Hinterberger [13]. The use of an incompressible flow solver is justified by the low Mach number in the experiment. LESOCC2 is a FORTRAN 95 program that allows for performing LES on body-fitted, collocated, curvilinear, block-structured grids. Both the viscous and convective fluxes are approximated with a second-order accurate central differences scheme. Time advancement is accomplished by an explicit, low-storage three-step Runge–Kutta method. Conservation of mass is achieved by the SIMPLE algorithm with the pressure–correction equation being computed with the strongly implicit procedure (SIP) of Stone. Velocity and pressure decoupling is avoided by a momentum interpolation technique. Since compressibility effects were neglected, a convection–diffusion transport equation is solved for the temperature. Hence, the temperature is treated as a passive scalar. Parallelization is achieved via domain decomposition with the use of ghost cells and MPI for the data transfer. The standard Smagorinsky model with $C_s = 0.1$ and van Driest wall-damping was employed as subgrid-scale model for the LES reported here. The turbulent Prandtl number was 0.7. Since the contribution of the subgrid-scale model is rather low, with values of ν_t/ν below 1, the choice of the subgrid-scale model is expected to have a small impact on the results. This was confirmed by comparison to significantly better resolved simulations.

2.3 Computational grid and averaging

All simulations were carried out on the same block-structured mesh containing about 38.2 million cells. Table 1 summarizes how the cells are distributed among the domains of the two precursor simulations and the main simulation. The bulk of the computational cells is allocated in the main simulation above the TE cutback, i.e. the area denoted as the region of interest in Fig. 1b. In the region of interest, 96 and 48 out of 288 cells were used to discretize the coolant channel and the cutback lip in the vertical direction, respectively. The grid was stretched towards the wall-normal direction to allow for wall-resolving simulations, and was equidistantly spaced in the streamwise and spanwise direction. The spanwise extent was $L_z = 8H$. Note that simulations with a span of $L_z = 4$ and $L_z = 12$ were also performed that yielded quite similar results with minor deviations in film cooling effectiveness' and second order statistics. However, the phenomena investigated here proved to be robust with respect to the variation of the span. Adaptive time-stepping ensured a CFL limit of less than 0.65 and yielded non-dimensional time-steps of $\Delta t \approx 0.6 - 1.0 \times 10^{-2}$. Each simulation was run for at least $150H/U_\mathrm{h}$, before starting averaging for $300H/U_\mathrm{h}$. In addition, spanwise averaging was applied over all 192 cells in the z-direction.

2.4 Boundary conditions and generation of inflow conditions

At all walls, the no-slip boundary condition (BC) was applied. The cold gas temperature was in accordance to the experiment and had a value of $T_\mathrm{c}/T_\mathrm{h} = 0.75$. A uniform temperature distribution was prescribed at the inflow boundaries. The lower wall had an adiabatic BC, whereas, for the walls confining the lip, an isothermal BC of $T_\mathrm{w}/T_\mathrm{h} = 0.86$ was enforced. At the upper domain boundary of the main simulation, a symmetry condition was enforced resulting in an adiabatic no-stress wall. At the outlet, a convective outlet BC was chosen for all variables. Furthermore, a buffer zone was used in which the viscosity is artificially increased. To prevent negative velocities at the outlet, a cosine function was employed that ramped the viscosity from ν_h to $10\nu_\mathrm{h}$ within the region of $x/H \in [17.5; 25]$.

In the context of LES, the generation of appropriate inlet BC for the filtered velocity field $\mathbf{u}(x, t)$ that satisfy the filtered Navier–Stokes equations and, at the same time, provide realistic turbulent flow structures is not a trivial task. Here, mean

Table 1 Details on the computational grid

	Precursor simulation I	Precursor simulation II	Region of interest
L_ξ	$12H$	$3H$	$15H$
L_η	$2H$	$1H$	$5H$
L_z	$8H$	$8H$	$8H$
N_ξ	160	48	480
N_η	96	96	288
N_z	192	192	192
N_total	2.9×10^6	0.9×10^6	26.5×10^6

L—length of domain, N—number of cells, indices ξ & η correspond to the streamwise and wall-normal directions, z corresponds to the lateral direction

values were prescribed and time-dependent fluctuations superimposed. At the hot gas inlet, the boundary layer profile was interpolated from the experimental data at the $x/H = 0$ location. The boundary layer had a thickness of $\delta = 2H$ and shape factor of $H_{12} = 1.5$. At the cold gas inlet, an equilibrium turbulent channel flow was imposed whose mass flux was matched to replicate the blowing ratio M. Note that the prescribed mean velocity profiles are likely to deviate somewhat from the (unknown) experimental values at the location of the inlet BC. The velocity fluctuations were generated by precursor simulations PS-I and PS-II that were running in parallel to the main simulation. These simulations were coupled by interfaces as can be seen in Fig 1b. Figure 2 gives an impression of the instantaneous flow field.

In both PS-I and II, periodicity was enforced in the streamwise direction and a controller was used to enforce the prescribed mass flux. This technique allows for the generation of fully-developed channel turbulence with physically realistic time-dependent flow structures. In PS-I, a half channel with half height $2H$ was computed using a symmetry condition at the upper boundary. In PS-II, a full channel with half height $H/2$ was simulated. The Reynolds number in the coolant channel is rather low and required a manipulation of the viscosity in PS-I and PS-II. The viscosity was set to $\nu_h/2$ in order to ensure fully-developed turbulence even for very low blowing ratios for which the coolant channel flow would be prone to relaminarization. Instantaneous data were extracted at every time-step and the local mean values $\mathbf{U} \equiv \overline{\mathbf{u}}$ were subtracted. The obtained fluctuating velocities $\mathbf{u}' = \mathbf{u} - \mathbf{U}$ were appropriately scaled and added to the prescribed mean values at the corresponding inlet BC of the main simulation. The rescaling operation was necessary in order to adjust the instantaneous fluctuations from PS-I and PS-II to the correct wall-shear of the main simulation. The rescaling technique was derived from the method proposed by Lund et al. [14] and contains some modifications specific to the setup here. The main differences are that, in our study, only the velocity fluctuations require the scaling and that the boundary layer thickness in the precursor and main simulations match. Furthermore, in the free-stream of the hot gas inlet (above $y/H = 2$), no fluctuations were added. To avoid a discontinuity between the instantaneous turbulent boundary layer and the calm free-stream, the rescaled fluctuations were attenuated towards the free-stream by using a cosine function in the region of $y/H \in [1.8; 2]$.

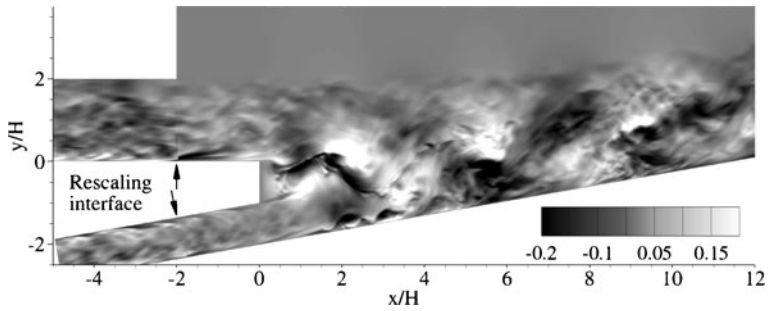

Fig. 2 Snapshot of LES for M = 0.8 at an arbitrary instant in time showing streamwise velocity u' fluctuation with flow from left to right. Precursor simulations for inlet data generation are located upstream of the rescaling interfaces

2.5 Simulation overview

In total, eight calculations are presented. The simulations were performed for eight different blowing ratios M = 0.35, 0.5, 0.65, 0.8, 0.95, 1.1, 1.25 and 1.4. For each blowing ratio, fully-developed turbulence was imposed as the cool gas BC. Since the flow is calculated as incompressible, M reduces with the consant temperature ratio $R_T = T_c/T_h = 0.75$ to a velocity ratio $U_c/U_h = M \cdot R_T$.

3 Results

3.1 Turbulent heat transfer

3.1.1 The counter-intuitive behavior

Before presenting the results of η_{aw} for the whole range of blowing ratios M considered here, it is instructive to briefly recall the counter-intuitive behavior of η_{aw} which was described in the study of Schneider et al. [12]. Figure 3a shows a linear-logarithmic distribution of the film cooling effectiveness η_{aw} along the streamwise coordinate x/H for a high (engine-typical) and low value of M = 1.1 and 0.5, respectively. The counter-intuitive behavior is that the case with the higher blowing ratio yields the lower cooling effectiveness.

In the literature, η_{aw} is typically plotted as $f(x/H)$ for a given M, where $f(\cdot)$ denotes the functional dependence. Such a representation was shown in Fig. 3a. There exists two interesting regions in which: (1) η_{aw} remains approximately constant, and (2) η_{aw} decays approximately exponentially. When comparing the results of the film cooling effectiveness for a wider range of blowing ratios, it is better to plot $\eta_{aw} = f(M)$ for a given streamwise location x/H. Figure 3b shows such an illustration for the entire range of blowing ratios at $x/H = 2$, 6, and 12. While η_{aw} maintains its maximum value of unity for all blowing ratios at $x/H = 2$, it shows a

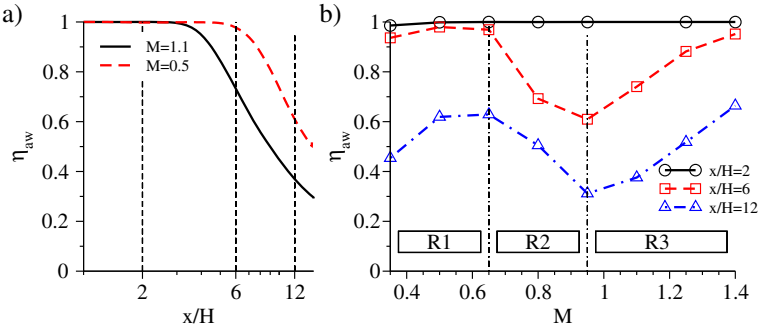

Fig. 3 Adiabatic film cooling effectiveness η_{aw} of LES. **a** Linear-logarithmic η_{aw}-distribution as function of streamwise coordinate x/H for selected blowing ratios M = 0.5 and 1.1. **b** η_{aw} distribution as function of M for $x/H = 2$, 6, and 12. *Dash-dotted lines* delimit regions R1, R2, and R3 comprising M ∈ [0.35; 0.65], M ∈ [0.65; 0.95], and M ∈ [0.95; 1.4], respectively

qualitatively different trend within three regions of M at $x/H = 6$ and 12. The three regions are denoted R1, R2, and R3, and approximately comprise M ∈ [0.35; 0.65], M ∈ [0.65; 0.95], and M ∈ [0.95; 1.4], respectively. In R1, η_{aw} increases for increasing M. This is intuitive as more cool gas should yield an improved cooling performance. In R2, however, η_{aw} decreases for increasing M. Paradoxically, more cool gas yields a reduced cooling performance. Clearly, the counter-intuitive behavior persists not only for one selected blowing ratio as in Fig. 3a, but rather for an entire range of blowing ratios. In R3, one observes again the expected behavior as the cooling effectiveness increases for increasing blowing ratios. Figure 3b illustrates that there exists two local extrema: a maximum and a minimum of η_{aw} in the vicinities of M = 0.65 and 0.95, respectively.

3.1.2 The η_{aw} map

We saw that it is possible to plot $\eta_{aw} = f(x/H)$ for selected M, or $\eta_{aw} = f(\mathrm{M})$ for selected x/H. However, neither representation is perfectly satisfactory since for a given configuration $\eta_{aw} = f(x/H, \mathrm{M})$. Therefore, a more comprehensive representation can be achieved by creating contours of η_{aw} with coordinates x/H and M. The advantage is that these contours provide a topology in which, like in a map, peaks and valleys can be easily identified. In the following, we demonstrate the usefulness of such maps and extend the concept to other quantities of interest.

Figure 4a shows an η_{aw}-map which was obtained by cubic interpolation of the LES data. The map reveals at a glance a characteristic topology. The features of this topology can be attributed to the counter-intuitive behavior which was described in the discussion of Fig. 3. The three regions R1, R2, and R3, as well as the local maximum and minimum of η_{aw} are visible for the whole range of x/H. The same η_{aw}-map has been created with the experimental data of Martini [10], see Fig. 4b. Clearly, the experimental data exhibit a similar topology with local performance maxima and minima. The interval comprising these extrema is, like in the LES, the region in which a counter-intuitive trend occurs. However, in the experiment, the levels of the

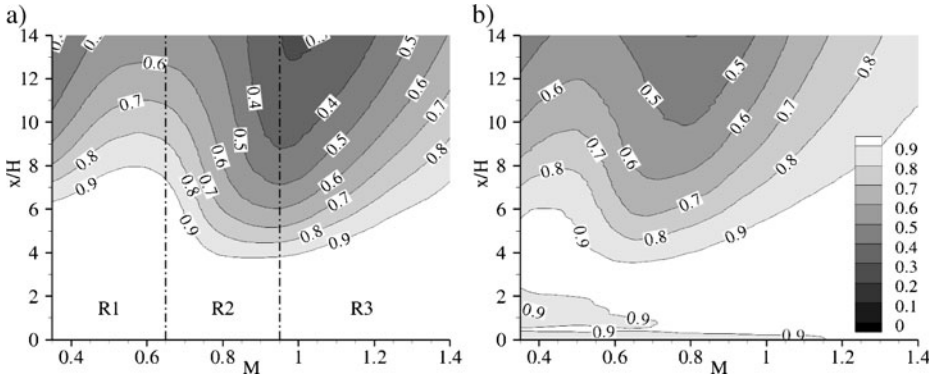

Fig. 4 Contours of adiabatic film cooling effectiveness η_{aw} of LES as function of blowing ratio M and streamwise coordinate x/H. **a** SIM-T data; *vertical dash-dotted lines* delimit regions R1, R2, and R3. **b** Experimental data of Martini [10]

local performance maxima and minima are less pronounced compared to the LES. Furthermore, the location of the interval is different and located at $M \in [0.5; 0.8]$.

Both the results from Martini [10] and Schneider et al. [12] showed that η_{aw} is highly sensitive to a variation in the boundary conditions. This allows for the conjecture that the differences between the experiments and the present LES shown in Fig. 4 are, at least partly, due to different boundary conditions and inherent simplifications of the setup. Recall that the present computational setup differs from the experiment, among other factors, by imposing (1) no free-stream turbulence in the hot gas path, (2) an estimated turbulent boundary layer profile in the hot gas path, (3) turbulent equilibrium flow in the coolant channel, (4) perfectly adiabatic BC along the TE cutback, (5) periodic BC in the lateral direction, (6) ideal geometric features, (7) passive scalar properties for the temperature, and (8) constant properties for the density and viscosity. Although differences between the computational and experimental setup exist, reasonably good qualitative agreement for η_{aw} was achieved, see Fig. 4. It is therefore conjectured that the current LES are well suited for further investigating the reasons for the characteristic topology of the η_{aw}-map.

Why is it so important to have an η_{aw}-map? One obvious reason is to know about the location of the optimum operating point. Another important reason is to identify critical operating points. Such a critical point would be $M = 0.8$ in the LES, which in fact lies between the local performance extrema. Around $M = 0.8$, strong gradients exist in the η_{aw}-map along the M coordinate and, hence, little changes in M can have a drastic impact on the performance of the coolant film.

3.1.3 Thermal mixing process

The topological features of the η_{aw}-map are related to the thermal mixing process in the near-wall region. This mixing process can be appreciated by analyzing the vertical temperature distribution. The dimensionless temperature Θ can be defined as

$$\Theta = \frac{T_h - T}{T_h - T_c}, \tag{3}$$

where T is the averaged temperature. It follows for the hot gas with T_h that $\Theta = 0$, for the cool gas with T_c that $\Theta = 1$, and for the wall with T_{aw} that $\Theta = \eta_{aw}$. The vertical distance from the wall is $y^* = (y - y_w)/H$, where y_w is the wall position. In order to better relate the wall temperature, as shown in the η_{aw}-map, to the thermal mixing process, we introduce a Θ-map; however, with coordinates y^* and M.

Figure 5a depicts a Θ-map in the near field of the cutback lip at $x/H = 2$, where $\eta_{aw} = 1$. It can be seen that Θ decreases from unity at the wall to zero in the free-stream. Moreover, the vertical Θ-distribution is strongly dependent on M. Again, the concept of the map proves to be an efficient means for identifying the characteristic topology of $\Theta = f(y^*, M)$. The features of the topology were highlighted by the solid bold Θ-levels which indicate $\Theta_h = 0 + \varepsilon$ (hot gas) and $\Theta_c = 1 - \varepsilon$ (cool gas), where ε is an arbitrarily chosen small number. The region in which $\partial\Theta/\partial y \neq 0$ is enclosed by the Θ_h and Θ_c contour lines and resembles a thermal mixing layer. However, the notion of a thermal mixing layer is, commonly, used in the context of free shear flows. Since our problem involves a wall, we instead adopt the notion of a thermal layer (TL) in order to describe, in a more general sense, the region in

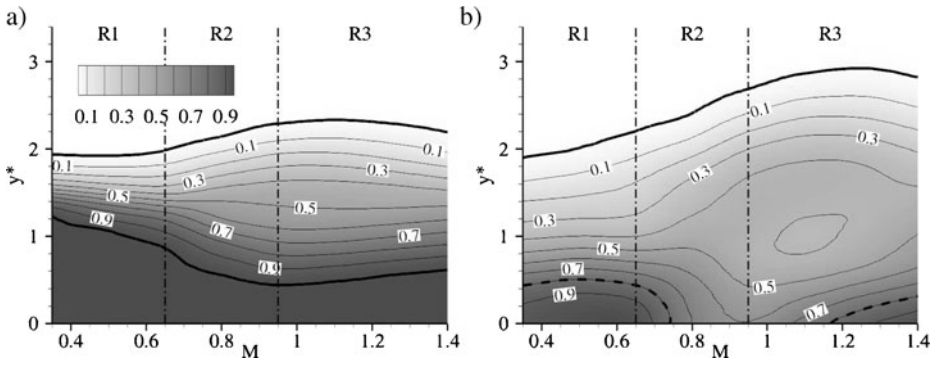

Fig. 5 Contours of dimensionless temperature Θ of LES as function of blowing ratio M and vertical wall-distance y^*; *vertical dash-dotted lines* delimit regions R1, R2, and R3. **a** Streamwise coordinate $x/H = 2$; *solid bold lines* indicate Θ_h and Θ_c. **b** $x/H = 6$; *solid bold line* indicates Θ_h and *dashed bold line* $\Theta = 0.8$

which $\partial\Theta/\partial y \neq 0$. The vertical location of the upper and lower boundaries of the TL are $\delta_h = y^*(\Theta_h, M)$ and $\delta_c = y^*(\Theta_c, M)$, respectively. Hence, the thickness of the TL is $\delta_{TL} = \delta_h - \delta_c$. Figure 5a illustrates that for increasing M, δ_{TL} increases within R1 and R2, and slightly decreases within R3. The strongest increase of δ_{TL} occurs within R2, and is due to a concomitant increase of δ_h and decrease of δ_c. Interestingly, the mixing process is strongest around M = 0.95: there exists a maximum of δ_{TL} and a minimum of δ_c.

Figure 5b shows the Θ-map for the far field of the cutback lip at $x/H = 6$, where $\eta_{aw} < 1$. Two major differences can be observed by comparing Fig. 3b to a: (1) Θ decreased below Θ_c, and (2) the topology of the Θ contours changed qualitatively. The consequences of $\Theta < \Theta_c$ are that $\delta_c = 0$. This implies, with our previous definition of the TL, that the TL extends from δ_h down to the adiabatic wall; thus $\delta_{TL} = \delta_h$. It can be seen that the thickness of the TL increased compared to the $x/H = 2$ location. Furthermore, δ_{TL} increases with increasing M and has its maximum in R3. We now turn attention to the qualitative change of the Θ topology. This change becomes visible when looking at the near-wall region with $y^* < 1$. The change of the Θ topology can be easily grasped by noting the dashed bold line which indicates the arbitrarily chosen value of $\Theta = 0.8$. Similarly as for the $x/H = 2$ location, the mixing process is strongest around M = 0.95: the Θ contours collapse in the vicinity of the wall.

The Θ-map showed that the mixing process was strongest for the same range of M = 0.95 where the η_{aw}-map had its minimum. The results suggest that the mixing process in the near field of the cutback lip is of great importance for the downstream cooling performance. Perhaps this may not be surprising; but what is not clear yet is why this enhanced mixing occurs in that specific range of M.

3.1.4 Turbulent heat fluxes

Both η_{aw} and Θ are averaged temperatures and, hence, provide us with the most fundamental description of the thermal field. The analysis of the thermal field can

be extended by scrutinizing the heat flux. The total heat flux vector $\mathbf{q}_{\mathrm{tot}}$ can be decomposed into a molecular $\mathbf{q}$ and a turbulent $\mathbf{q}_{\mathrm{t}}$ contribution:

$$\mathbf{q}_{\mathrm{tot}} = \mathbf{q} + \mathbf{q}_{\mathrm{t}}. \tag{4}$$

Analysis of the present data showed that, in the near-field of the cutback lip, $\mathbf{q}_{\mathrm{t}}$ is up to four orders of magnitude larger than $\mathbf{q}$. It follows that the temperature transport is significantly influenced by the fluctuating velocity field. In order to relate the thermal mixing process in the near-wall region, as shown in the Θ-map, to the turbulent heat fluxes, we introduce a $\mathbf{q}_{\mathrm{t}}$-map with coordinates y^* and M. Since $\mathbf{q}_{\mathrm{t}}$ is a vector quantity, it is necessary to create a map for the two non-zero components of $\mathbf{q}_{\mathrm{t}}$: the streamwise $\overline{u'T'}/U_{\mathrm{h}}T_{\mathrm{h}}$ and the vertical $\overline{v'T'}/U_{\mathrm{h}}T_{\mathrm{h}}$ component. Note that for the sake of brevity the normalization factor $U_{\mathrm{h}}T_{\mathrm{h}}$ is omitted in the following.

Figure 6 illustrates the $\overline{u'T'}$-map (top) and $\overline{v'T'}$-map (bottom) for the two streamwise locations $x/H = 2$ and 6. Similarly as in Fig. 5, the boundaries of the TL were highlighted by Θ_{h} and Θ_{c}. Furthermore, the Θ-collapse was highlighted by $\Theta = 0.8$ for $x/H = 6$. For both streamwise locations, the turbulent heat fluxes are non-zero within the TL and zero outside the TL. This is consistent with $\mathbf{q}_{\mathrm{t}} \gg \mathbf{q}$ and shows the

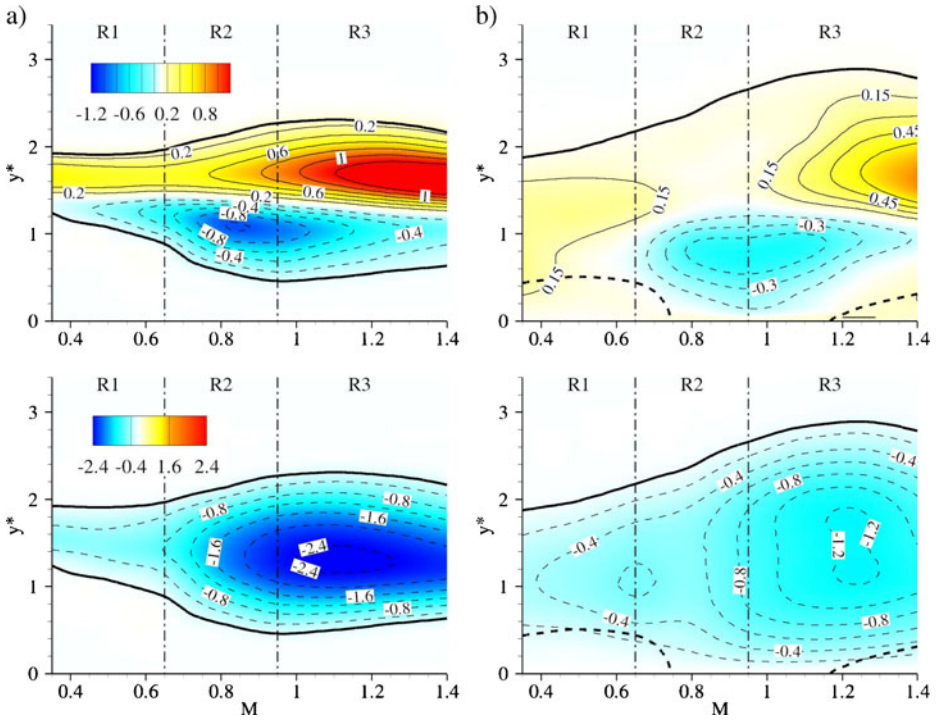

Fig. 6 Contours of resolved streamwise $100 \times \overline{u'T'}/U_{\mathrm{h}}T_{\mathrm{h}}$ (*top*) and vertical $100 \times \overline{v'T'}/U_{\mathrm{h}}T_{\mathrm{h}}$ (*bottom*) turbulent heat flux components of LES as function of the blowing ratio M and vertical wall-distance y^*; same color contours shown with different contour lines, *dashed contour lines* indicate negative values; *vertical dash-dotted lines* delimit regions R1, R2, and R3. **a** Streamwise coordinate $x/H = 2$; *solid bold lines* indicate Θ_{h} and Θ_{c} contour levels. **b** $x/H = 6$; *solid bold line* indicates Θ_{h} and *dashed bold line* $\Theta = 0.8$

turbulent heat fluxes are dominating the thermal mixing process. First, we inspect the $\overline{v'T'}$-maps (bottom figures). The maps show that only negative values of $\overline{v'T'}$ occur within the TL. This means that heat is transported towards the wall which explains the deterioration of the cooling film. From our previous findings, one could presume that the maximum vertical heat transfer then should coincide with the Θ-collapse around M = 0.95. However, maximum values of negative $\overline{v'T'}$ can be observed for M ≥ 1.1; and not for M = 0.95. Apparently, it is not sufficient to look at the vertical component $\overline{v'T'}$ alone. This becomes clear by noting that although $\overline{v'T'} > \overline{u'T'}$, both components are of the same order of magnitude. Therefore, one has to consider the streamwise component $\overline{u'T'}$ as well. The $\overline{u'T'}$-maps (top figures) show that there exists both positive and negative values within the TL. Note that negative values of $\overline{u'T'}$ correspond to an upstream transport of heat. The $\overline{u'T'}$-map in Fig. 6b reveals at a glance that strong negative values of $\overline{u'T'}$ occur for $y^* < 1$ in the region around M = 0.95. That is in the exact same region of M for which the Θ-collapse and the associated counter-intuitive behavior of η_{aw} occurs.

We now relate the combined contribution of $\overline{u'T'}$ and $\overline{v'T'}$ to the Θ-collapse at $x/H = 6$. Figure 7 presents the corresponding $\mathbf{q}_t$-vectors in the near-wall region for selected M. The figure visualizes that (1) the angle of incidence, and (2) the magnitude of $\mathbf{q}_t$ vary with the vertical wall-distance. The $\mathbf{q}_t$-distribution for M = 0.95 shows that the Θ-collapse can be attributed to both strong negative $\overline{u'T'}$ and strong negative $\overline{v'T'}$ that extend very close to the wall. Similar observations can be made for the $\mathbf{q}_t$-distribution of M = 0.8 and 1.1. In contrast, the other cases for which the mixing is less intense are characterized by either low magnitudes of $\mathbf{q}_t$, as in M = 0.65, or by a positive streamwise component $\overline{u'T'}$, as in M ≥ 1.25. Hence, the strongest thermal mixing is due to a turbulent heat flux vector that carries heat not only towards the wall, but also in the upstream direction.

3.2 Large coherent structures

The previous analysis demonstrated that the counter-intuitive behavior of η_{aw} was caused by a particular composition of the turbulent heat flux vector in the near-wall region: both the vertical and the streamwise components were negative. In order to

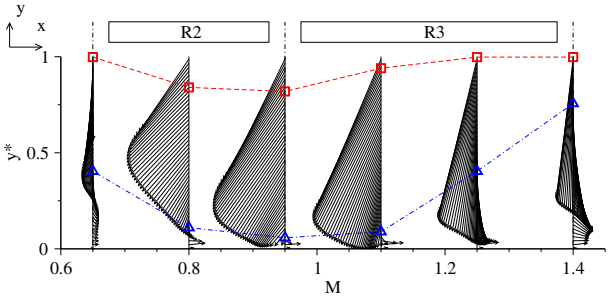

Fig. 7 Turbulent heat flux vectors $\mathbf{q}_t$ of LES in the near-wall region for selected blowing ratios M at $x/H = 6$; *square* linked by *dashed line* refers to location of maximum magnitude of $\mathbf{q}_t$ and *triangles* linked by the *dashed-dotted line* refers to change in sign of *x*-component of $\mathbf{q}_t$ vector; *vertical dash-dotted lines* delimit regions R2 and R3 comprising M ∈ [0.65; 0.95] and M ∈ [0.95; 1.4], respectively. Flow is in positive *x*-direction, see coordinate system

understand the origin of this particularity, we inspect the turbulent flow field which gives rise to the turbulent heat fluxes.

3.2.1 Flow field statistics

First, we give an impression of the flow field by providing profiles at selected streamwise locations for a single M. Profiles for other M together with a detailed comparison with the experimental results can be found in Schneider et al. [12]. Figure 8 shows major flow field quantities for M = 0.8 at the streamwise locations $x/H = 0$, 2, and 6. The mean streamwise U/U_h velocitiy, the streamwise $u_\mathrm{rms}/U_\mathrm{h}$ and vertical $v_\mathrm{rms}/U_\mathrm{h}$ r.m.s. velocities, as well as the Reynolds shear-stress $\overline{u'v'}/U_\mathrm{h}^2$ are plotted against y^*. Note that the normalization factors will be omitted in the following. The r.m.s. velocity is defined as the variance of the velocity fluctuation, e.g. in the streamwise direction $u_\mathrm{rms} \equiv (\overline{u'u'})^{1/2}$. Hence, the r.m.s. velocities correspond to a normal Reynolds stress. Also note that the mean velocity in the spanwise direction, as well as the remaining Reynolds shear-stress components are zero due to the periodicity in the spanwise direction. As discussed in Section 3.1.2, there are differences in the setup between the simulation and the experiments. Nevertheless, it can be seen that the simulation and the experiment are in reasonably good qualitative agreement. In summary, the simulation is able to replicate the major flow-field characteristics of the experiment.

So far, the concept of the map proved valuable. This suggests to transfer its concept to the Reynolds stresses – with the aim to identify a characteristic topology. In this way, it may be possible to relate the Reynolds stresses to the turbulent heat fluxes. Figure 9 shows the $\overline{u'u'}$-map (top), the $\overline{v'v'}$-map (middle), and the $\overline{u'v'}$-map (bottom) for the two streamwise locations $x/H = 2$ and 6. First, we look at the stresses at $x/H = 2$ in Fig. 9a. For increasing M, the $\overline{u'u'}$ contours reveal the emergence of a double peak within the TL, and a single peak below the TL. On the

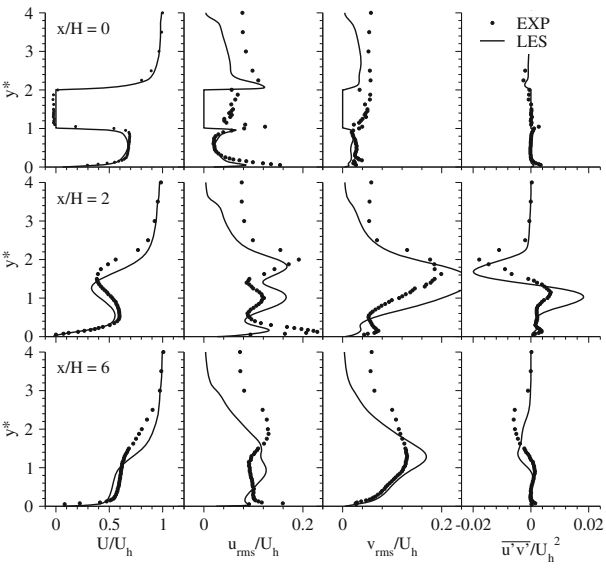

Fig. 8 Flow field statistics of LES and experimental data of Martini [10] for M = 0.8. From *top to bottom*: $x/H = 0$, 2, and 6; from *left to right*: mean streamwise U/U_h velocity, corresponding resolved streamwise $u_\mathrm{rms}/U_\mathrm{h}$ and vertical $v_\mathrm{rms}/U_\mathrm{h}$ velocities, and resolved shear-stress component $\overline{u'v'}/U_\mathrm{h}^2$

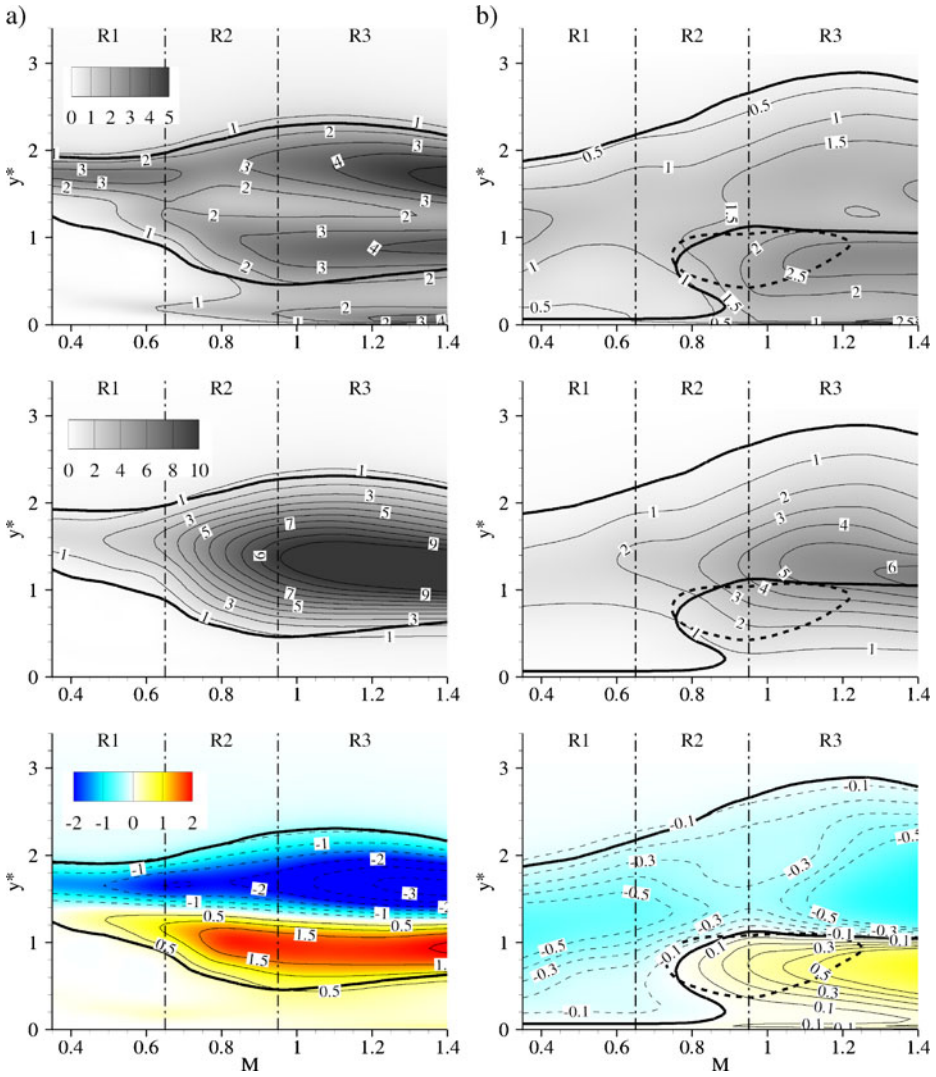

Fig. 9 Contours of resolved streamwise $100 \times \overline{u'u'}/U_h^2$ (*top*) and vertical $100 \times \overline{v'v'}/U_h^2$ (*middle*) Reynolds stresses, and shear-stress component $100 \times \overline{u'v'}/U_h^2$ (*bottom*) of LES as function of the blowing ratio M and vertical wall-distance y^*; same color contours shown with different contour lines, *dashed contour lines* indicate negative values; *vertical dash-dotted lines* delimit regions R1, R2, and R3. **a** Streamwise coordinate $x/H = 2$; *solid bold lines* indicate Θ_h and Θ_c contour levels. **b** $x/H = 6$; *solid bold lines* indicate Θ_h (*upper line*) and $\overline{u'v'}/U_h^2 = 0$ (*lower line*), and *dashed bold line* $\overline{u'T'}/U_h T_h = -0.3$

other hand, the $\overline{v'v'}$ contours testify for a single peak within the TL. The $\overline{u'v'}$ contours show that there exists negative values in the upper part of the TL, and positive values in the lower part of the TL. It can be seen that the magnitude of all stresses increases for increasing M.

From the above it is yet difficult to determine a relation between the Reynolds stresses and the turbulent heat fluxes. That there exists such a relation can be conjectured by appreciating the characteristic topology of the $\overline{u'v'}$-map for $x/H = 6$, as shown in Fig. 9b. Similarly as for $x/H = 2$, negative values of $\overline{u'v'}$ can be observed in the upper part of the TL. However, instead of observing only positive values of $\overline{u'v'}$ in the lower part of the TL, we observe both positive and negative values in the near-wall region with $y^* < 1$. The negative values of $\overline{u'v'}$ are found in R1, while the positive values are found in R3. Interestingly, $\overline{u'v'}$ changes its sign in R2. Indeed, it is this change of sign which partially coincides with a region of negative values of $\overline{u'T'}$. The coincidence becomes clear by examining the $\overline{u'v'} = 0$ and $\overline{u'T'} = -0.3$ contour levels that were highlighted in Fig. 9b. Hence, by considering only R1 and R2, the data suggest that the change of sign from negative to positive values of $\overline{u'v'}$ correlates somehow with the emergence of negative values of $\overline{u'T'}$. But when considering R2 and R3, no such correlation can be observed. Here, $\overline{u'v'}$ keeps its sign although $\overline{u'T'}$ becomes positive for increasing values of M, see Fig. 6b. Moreover, $\overline{u'v'}$ even increases in magnitude. A similar increase in magnitude is visible for $\overline{u'u'}$ and $\overline{v'v'}$. Apparently, it is not possible to unambiguously relate the Reynolds stresses to the turbulent heat fluxes.

3.2.2 Instantaneous flow structures

The work of Schneider et al. [12] demonstrated that for the two M considered, i.e. M = 0.5 in R1 and M = 1.1 in R3, different kinds of LCS were formed. It was found that both the kind and the strength of these LCS determined the mixing process. In the remaining section, we will visualize instantaneous LCS in order to attempt locating the region of the counter-intuitive behavior. Differences in the type and strength of the LCS, and in the resulting flow field facilitate an explanation for the variations in the cooling performance.

Figure 10 shows flow structures for five selected cases of M. The cases were selected according to the three regions R1, R2, and R3 of the η_{aw}-map: M = 0.5 (in R1), 0.65 (performance maximum connecting R1 and R2), 0.95 (performance minimum connecting R2 and R3), 1.25 and 1.4 (in R3). As suggested in von Terzi et al. [15], the large-scale structures are visualized by iso-contours of the pressure fluctuation p', and the small-scale structures are visualized by iso-contours of the vortex identification criterion Q. The latter is defined as

$$Q = \frac{1}{2}\left(W_{ij}W_{ij} - S_{ij}S_{ij}\right), \tag{5}$$

where W_{ij} is the rate of rotation and S_{ij} the rate of strain of the instantaneous velocity field. Furthermore, color contours of the temperature are included at a vertical plane at $z/H = 0$ and at the lower wall which, in the present incompressible LES, visualize flow patterns similar to dye in water experiments.

In a first step, we scrutinize the LCS which are formed for the performance minimum at M = 0.95. For this M, a line of large-scale clockwise-rotating structures (C-S), i.e. spanwise rollers, can be identified. In between the rollers, there exists small-scale braid-like structures, which are aligned predominantly in the streamwise direction. The strength of the small-scale structures decreases with increasing distance from the cutback lip. Inspection of the T/T_{h} contours reveals the importance of the LCS for the turbulent heat transfer: as the C-S convect downstream, they

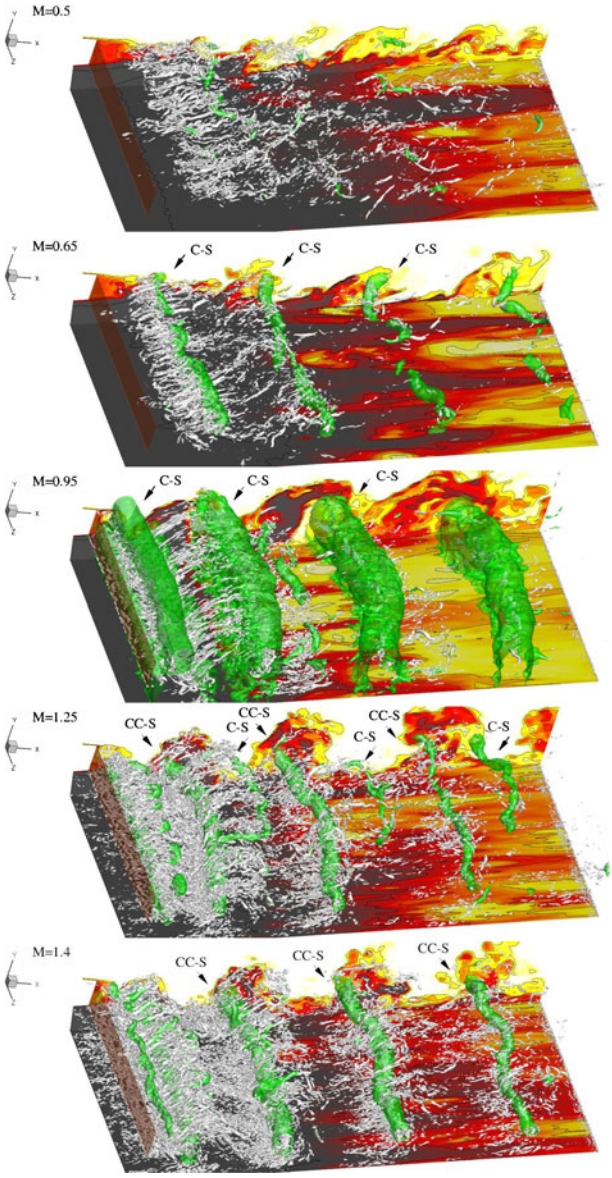

Fig. 10 Snapshots of LES for selected M at an arbitrary instant in time showing the near-wall part of the computational domain along the TE cutback: large-scale structures visualized by iso-contours of pressure fluctuation $p' = -0.075$ (*green*); small-scale structures visualized by iso-contours of vortex identification criterion $Q = 7.5$ (*grey*); vertical slice at $z/H = 0$ and at the lower wall visualized by color contours of the temperature T/T_h; lip of TE cutback is indicated by the *red rectangle*

entrain large quantities of hot-gas fluid towards the wall and, at the same time, cold-gas fluid towards the free-stream. This is more clearly illustrated in Fig. 11a, where the corresponding spanwise-averaged snapshot of the temperature contours is shown. It can be seen that each C-S transports a package of mixed hot- and cold-gas fluid that resembles the crest of a breaking wave. The fundamental relationship between the turbulent flow field and the turbulent heat fluxes can be understood by examining Fig. 11b. This figure presents a spanwise-averaged snapshot of both the temperature and the velocity fluctuations. The strong rotational motion of the C-S

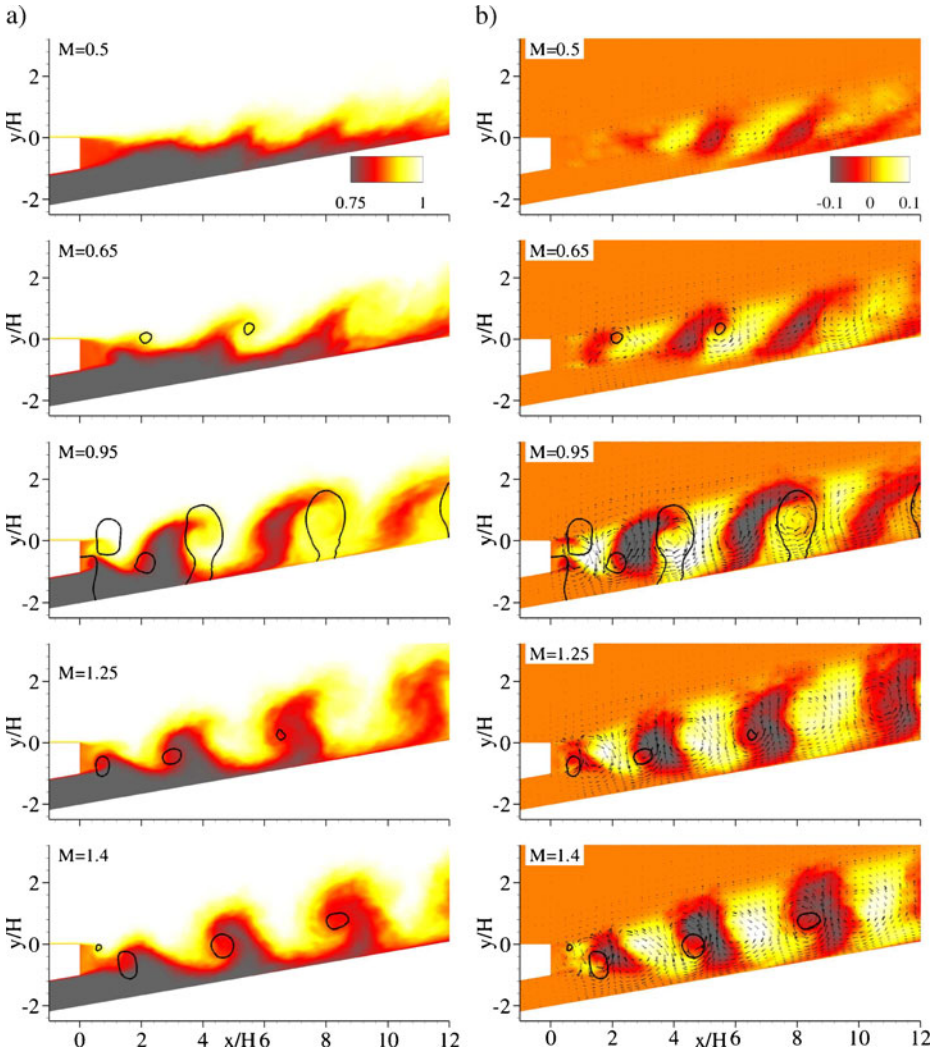

Fig. 11 Spanwise-averaged snapshot of LES for selected M at an arbitrary instant in time (same instant as in Fig. 10). **a** Instantaneous temperature T/T_h contours with superimposed lines of pressure fluctuation $p' = -0.075$. **b** Temperature fluctuation T'/T_h contours with superimposed lines of pressure fluctuation $p' = -0.075$ and velocity fluctuation vectors; every nineth and twelfth vector in the streamwise and *vertical directions* shown, respectively

causes a clockwise roll-up of the temperature, see for an illustrative example the C-S which is located around $x/H = 8$. Eventually, the roll-up is so strong that positive temperature fluctuations are transported in the upstream direction and towards the wall. This is the mechanism that causes the upstream directed heat flux which gives rise to the enhanced mixing in the region of the counter-intuitive behavior of η_{aw}.

In a second step, we scrutinize the change in LCS for a decrease of M departing from M = 0.95. Recall that in R2 between M = 0.95 and 0.65 the drastic performance change in the η_{aw}-map occurred, see Fig. 4a. Hence, one could presume that this

drastic performance change is caused by a drastic change in the flow structures. However, when scrutinizing the LCS for the performance maximum at M = 0.65, both similarities and drastic differences can be observed. The most striking similarity is the existence of only the large-scale C-S. The differences become clear by looking at the strength of these structures and by closely inspecting the shape of the temperature patterns in Fig. 11a. The T/T_h contours reveal that the wave-like patterns are less pronounced compared to the M = 0.95 case. This is confirmed in Fig. 11b which illustrates that the fluctuations are rather weak. Consequently, the C-S have a weaker rotational moment and transport less heat towards the wall. For completeness, it should be noted that a further decrease to M = 0.5 causes a further weakening of the C-S. Eventually, when M is as low as 0.35 (not shown), the C-S break down already after the first shedding cycle. This breakdown is associated with the generation of a large number of smaller structures that are sustained at higher intensity levels farther downstream. For this case, the mixing process is apparently dominated by the smaller scales rather than by the larger ones.

Next, we look at the change in LCS for an increase of M, again starting from M = 0.95. An increase to M = 1.25 results in a qualitative change in the kinds of LCS that are formed. For this case, we identify staggered pairs of C-S and counter-clockwise rotating structures (CC-S). While the CC-S is stronger and extends over the entire span, the C-S is weaker and extends only over part of the span. Each pair of C-S and CC-S transports the packages of mixed hot- and cold-gas fluid. In contrast to the cases for M $\leq$ 0.95, these packages form mushroom-like patterns rather than wave-like patterns in the T/T_h contours, see also Fig. 11a. Again, the reason becomes clear by inspecting the fluctuations which are shown in Fig. 11b. It can be seen that the lower CC-S obstructs the transport of heat towards the wall by the upper C-S, see the pair which is located around $x/H = 7$. This is concomitant with a net transport of heat in the downstream direction that correlates with an improved film-cooling effectiveness compared to M = 0.95. When M is further increased to M = 1.4, the wave-form appears again, but oriented in the reverse direction as shown in Fig. 11a. For this M, the temperature patterns are transported exclusively by the CC-S. The mechanism for the heat transfer here is essentially the same as in R2, but weaker since the upstream directive component of turbulent heat flux is missing.

From the above it should be noted that the sole identification of the kind of LCS is not sufficient to properly assess their impact on heat transfer. While it was possible to discern R2 and R3 by the change in the kind of LCS being formed, this was not possible for R1 and R2. The reason is that not only the kind, but also the strength of the LCS determine the heat transfer. More importantly, the data imply that similar flow structures can yield very different η_{aw} distributions (M = 0.65 versus 0.95). Conversely, it is also possible that very different flow structures can yield similar η_{aw} distributions (M = 0.35 versus 1.25).

4 Conclusions

The interrelationship between turbulent heat transfer and large coherent structures in a film-cooled trailing-edge cutback section from a turbine airfoil was investigated through well-resolved LES. The objective of the present study was to elucidate the physical mechanisms causing a counter-intuitive decrease of the film-cooling

effectiveness η_{aw} for an increase in the blowing ratio M, which was observed in previous simulations and experiments.

In total, eight simulations with the blowing ratio varying as the only parameter were conducted over a range from $M = 0.35$ to 1.4. The computational setup is of practical interest as it replicated the geometry and Reynolds number of a corresponding experiment that was designed according to specifications from the turbomachinery industry. Time-dependent realistic inflow data were generated and appropriately rescaled to match the experimental inflow conditions. The computational setup was validated by a detailed comparison with experimental data in Schneider et al. [12], and supplementary data were shown here. Although deviations between the simulations and the experiments exist, these were consistently explained and it was deduced that the adopted approach captured the statistical characteristics of the flow and heat transfer. These characteristics were visualized by maps, which facilitated the statistical analysis for the wide range of blowing ratios considered here.

From the identification and analysis of the large coherent structures being formed behind the cutback lip, we found evidence that dominant clockwise-rotating flow structures existed in the region of M in which the counter-intuitive behavior occurred. The statistical data suggested that these distinct LCS gave rise to a strong upstream- and wall-directed turbulent heat flux, which represented the main contribution of the total heat flux. This turbulent heat flux yielded the significantly enhanced thermal mixing process in the near-wall region that was concomitant with the excessive deterioration of the film cooling effectiveness. Therefore, the present work identified a possible mechanism that causes the counter-intuitive behavior of η_{aw}.

Acknowledgements The work reported here was carried out within the "Research Group Turbo-DNS" at the Institut für Thermische Strömungsmaschinen. Its financial support by means of the German Excellence Initiative and Rolls–Royce Deutschland is gratefully acknowledged. The authors are grateful for the provision of computer time by Steinbuch Centre for Computing (SCC) Karlsruhe and Leibniz Computing Centre (LRZ) Munich, and to Dr. Patrick Martini for making the experimental data available.

References

1. Bunker, R.S.: Cooling design analysis. DOE–NETL, The Gas Turbine Handbook. http://www.netl.doe.gov/technologies/coalpower/turbines/refshelf/handbook/TableofContents. (2006). Accessed 30 August 2010
2. Holloway, D.S., Leylek, J.H., Buck, F.A.: Pressure Side Bleed Film Cooling: Part I–Steady Framework for Experimental and Computational Results. ASME Paper No. GT–2002–30471 (2002)
3. Holloway, D.S., Leylek, J.H., Buck, F.A.: Pressure Side Bleed Film Cooling: Part II–Steady Framework for Experimental and Computational Results. ASME Paper No. GT–2002–30472 (2002)
4. Medic, G., Durbin, P.A.: Unsteady effects on trailing edge cooling. J. Heat Transfer **127**, 388–392 (2005)
5. Joo, J., Durbin, P.A.: Simulation of turbine blade trailing edge cooling. ASME J. Fluids Eng. **131** (2009). doi:10.1115/1.3054287
6. Martini, P., Schulz, A., Bauer, H.-J., Whitney, C.F.: Detached Eddy simulation of film cooling performance on the trailing edge cutback of gas turbine airfoils. ASME J. Turbomach. **128**, 292–300 (2006)
7. Pope, S.B.: Turbulent Flows. Cambridge University Press, Cambridge (2000)
8. Fröhlich, J., von Terzi, D.A.: Hybrid LES/RANS methods for the simulation of turbulent flows. Prog. Aerosp. Sci. **44**, 349–377 (2008)

9. Martini, P., Schulz, A., Bauer, H.-J.: Film cooling effectiveness and heat transfer on the trailing edge cutback of gas turbine airfoils with various internal cooling designs. ASME J. Turbomach. **128**, 196–206 (2006)
10. Martini, P.: Filmkühlung hoch-beanspruchter Turbinen-schaufel-hinter-kanten: Wärme-übergang und Strömung im Nahfeld praxis-bezogener Ausblase-spalte. Dissertation, University of Karls-ruhe, Karlsruhe, Germany (2008)
11. Horbach, T., Schulz, A., Bauer, H.-J.: Trailing edge film cooling of gas turbine airfoils—external cooling performance of various internal pin fin configurations. ASME J. Turbomach. **133** (2011). doi:10.1115/1.4002964
12. Schneider, H., von Terzi, D.A., Bauer, H.-J.: Large–Eddy simulations of trailing-edge cut-back film cooling at low blowing ratio. Int. J. Heat Fluid Flow **31**, 767–775 (2010). doi:10.1016/j.ijheatfluidflow.2010.06.010
13. Hinterberger, C.: Dreidimensionale und tiefengemittelte Large–Eddy-Simulation von Flachwasser-strömungen. Dissertation, University of Karls-ruhe, Karlsruhe, Germany (2004)
14. Lund,T.S., Wu, X., Squires, K.D.: Generation of turbulent inflow data for spatially-developing boundary layer simulations. J. Comput. Phys. **140**, 233–258 (1998)
15. von Terzi, D.A., Sandberg, R.D., Fasel, H.F.: Identification of large coherent structures in supersonic axisymmetric wakes. Comput. Fluids **38**, 1638–1650 (2009)